MODELING AND OPTIMIZATION OF HYBRID SOLAR THERMOELECTRIC SYSTEMS WITH THERMOSYPHONS

Nenad Miljkovic and Evelyn N. Wang*
Device Research Laboratory
77 Massachusetts Avenue, 3-461
Department of Mechanical Engineering
Massachusetts Institute of Technology
Cambridge, MA, 02139, USA

*Corresponding Author
Evelyn Wang
Department of Mechanical Engineering,
Massachusetts Institute of Technology,
77 Massachusetts Avenue, 3-461B
Cambridge, MA, 02139, USA
Tel: 1-617-324-311
Email:enwang@mit.edu

ABSTRACT

We present the modeling and optimization of a new hybrid solar thermoelectric (HSTE) system which uses a thermosyphon to passively transfer heat to a bottoming cycle for various applications. A parabolic trough mirror concentrates solar energy onto a selective surface coated thermoelectric to produce electrical power. Meanwhile, a thermosyphon adjacent to the back side of the thermoelectric maintains the temperature of the cold junction and carries the remaining thermal energy to a bottoming cycle. Bismuth telluride, lead telluride, and silicon germanium thermoelectrics were studied with copper-water, stainless steel-mercury, and nickel-liquid potassium thermosyphon-working fluid combinations. An energy-based model of the HSTE system with a thermal resistance network was developed to determine overall performance. In addition, the HSTE system efficiency was investigated for temperatures of 300 K – 1200 K, solar concentrations of 1 – 100 suns, and different thermosyphon and thermoelectric materials with a geometry resembling an evacuated tube solar collector. Optimizations of the HSTE show ideal system efficiencies as high as 52.6% can be achieved at solar concentrations of 100 suns and bottoming cycle temperatures of 776 K. For solar concentrations less than 4 suns, systems with thermosyphon wall thermal conductivities as low as 1.2 W/mK have comparable efficiencies to that of high conductivity material thermosyphons, *i.e.* copper, which suggests that lower cost materials including glass can be used. This work provides guidelines for the design, as well as the optimization and selection of thermoelectric and thermosyphon components for future high performance HSTE systems.

KEYWORDS: hybrid solar thermoelectric, bottoming cycle, solar thermal, thermosyphon

1. INTRODUCTION

Efficient renewable energy sources are in significant demand to replace diminishing and environmentally harmful fossil fuels. The combination of commercial and residential buildings as well as the industrial sector currently consumes 72% of the total energy in the US (Davidson, 2005; Kelso, 2009). A significant portion of this energy is used in the form of heat, such as for hot water heaters in homes and food processing in industrial process heat (IPH) applications, where temperatures range from 50 ^{o}C to 1000 ^{o}C (Desideri et al., 2009; Demeter et al., 1991; Schnitzer et al., 2007; Lecuona et al., 2009). The abundance of solar energy promises efficient methods to meet the current heating and electricity needs. For example, hot water heaters have been commonly used in households (Han et al., 2010; Zhiqiang, 2005), and large scale solar thermal plants deliver distributed electrical power to cities (Manuel et al., 2002; Pacheco, 2001). In most cases, however, these systems are limited to providing either heat or electricity. More recently, hybrid systems with either photovoltaics or thermoelectrics to generate both electrical power and heat have been investigated. Hybrid photovoltaic-thermal (PVT) systems (Tripanagnostopoulos et al., 2002; Dubey and Tiwari, 2008; Garg and Adhikari, 1999; Shahsavar and Ameri, 2010; Chowdhury et al., 2010; Kribus and Mittelman, 2008) use photovoltaics (PV) to generate power, but are limited to low temperature (30 ^{o}C – 80 ^{o}C) waste heat production. Concentrating hybrid photovoltaic-thermal (CPVT) systems (Gibart, 1981; Buffet, 1982; Zondag, 2005; Coventry, 2004; Rosell et al., 2005; Tripanagnostopoulos, 2007) show higher electrical conversion efficiencies than PVT systems but are also limited to low temperature operation. In these systems, there is a significant degradation in electrical conversion efficiency when temperatures increase due to higher internal carrier recombination in the PV (Green, 2003; Luque and Marti, 1999).

Thermoelectrics (TE), in contrast, promise higher electrical conversion efficiencies at elevated operating temperatures because thermal energy is directly converted to electrical energy *via* the Seebeck effect. When a temperature difference exists across the TE, power is produced with no moving parts. Solar TE energy conversion systems (Lenoir et al., 2003; Omer and Infield, 1998; Xi et al., 2007; Deng and Liu, 2009; Rockendorf et al., 1999; Muto and Chen, 2010; Kramer et al., 2011; Chen, 2011), where solar energy drives the temperature difference across the TE, have significant potential to produce electrical energy with abundant waste heat to meet building energy or IPH demands. Rockendorf *et al.* (1999) and Li *et al.* (2010) investigated hybrid solar TE water heaters and numerically determined that low radiative losses and efficient back side cooling are needed to attain electrical conversion efficiencies up to 30% of the Carnot efficiency. However, Lertsatitthanakorn *et al.* (2010) experimentally showed that hybrid solar TE water heaters with backside cooling have efficiencies limited to 0.87% due to electrical pumping requirements. The results of these studies suggest that the development of more efficient cooling methods for the TE back side is needed to realize the potential of hybrid TE systems. In addition, parametric optimizations could extend the utilization of waste heat from hot water systems to a variety of applications that require a larger range of temperatures.

In this work, we investigated the design of a hybrid solar TE system where a thermosyphon passively and efficiently transfers heat to a secondary (bottoming cycle) application for low temperature water heating or higher temperature

co-generation and IPH. In addition, thermosyphons are reliable and can be used for a large range of temperatures (Faghri, 1995). Figure 1 shows the hybrid solar thermoelectric (HSTE) configuration we studied in this work. A parabolic concentrator focuses light on the evaporator section of the evacuated tube absorber (thermosyphon), heating the TE hot side located on the inner tube. The resulting temperature gradient between the TE hot and cold sides produces electrical power. Meanwhile, the thermosyphon interfaced on the TE cold side maintains the temperature and transfers the heat (waste heat) to the condenser section for co-generation, IPH, or hot water heating.

[Figure 1]

We developed an energy-based model to investigate the effect of solar concentration, TE and thermosyphon material and geometry, thermosyphon working fluid, and bottoming cycle temperatures on HSTE system performance (Section 2). The results from the model are subsequently used to i) optimize the HSTE efficiency and radial geometry, ii) investigate the effect of different thermal conductivity thermosyphon wall materials to potentially reduce cost, and iii) propose potential commercial applications for HSTE utilization (Section 3). The outcomes of this work aid in predicting the performance of five potential solar applications and provide guidelines for the design, optimization and selection of TE and thermosyphon components for future high performance HSTE systems.

2. MODEL

2.1 MODEL FORMULATION

A cross-sectional schematic with the geometric parameters of the HSTE and the equivalent thermal resistance model (Prasher, 2003; Tundee et al., 2010) are shown in Figures 2a and 2b, respectively. A solar parabolic concentrator (Figure 1) focuses sunlight (Q_{solar}) on a selective surface (SS) with a low thermal emissivity and high solar absorbtivity. The surface also emits thermal radiation (Q_{loss}) at a spectrally averaged emissivity (ε) due to its elevated temperature (T_{ss}). To accurately capture the absorptive and emissive properties, NREL data was used for four thermally and mechanically robust commercially available surface coatings (Kennedy and Price, 2006) (see Appendix). The selective surface is assumed to be isothermal along its length, and the temperature drop from the SS to the TE hot side is across a thin film (< 500 μm) and therefore can be neglected (Chen, 2011). We also assumed that in the evacuated concentric tube design there are only radiative losses from the selective surface.

[Figure 2]

The net heat absorbed by the SS is conducted through the TE element with a radial conduction thermal resistance R_{te}, which leads to a temperature gradient between the TE hot (T_{ss}) and cold ($T_{s,E}$) side to produce TE power (P_{te}). The temperature gradient is dependent on the TE leg geometry, material thermal conductivity (k_{te}), and figure of merit (ZT). Due to the high sensitivity of these parameters on system performance, temperature dependent properties were used for the TE thermal conductivity (Figure 3a) and figure of merit (Figure 3b) (Minnich et al., 2009; Poudel et al., 2008; Snyder and Toberer, 2008; A.A. El-Sharkawy, 1983; Morelli et al., 2008).

[Figure 3]

An inclined two-phase thermosyphon in contact with the TE cold side transfers heat (Q_{out}) axially to the bottoming cycle application at a temperature T_c. The thermosyphon achieves efficient spreading *via* a working fluid that undergoes phase-change due to the heat supplied to the evaporator. The generated vapor axially transports to the condenser section. As heat is transferred to the bottoming cycle application, the vapor condenses and returns back to the evaporator by gravity. The heat transfer processes in the thermosyphon are modeled as thermal resistances (Figure 2b): R_1 and R_6 are the radial conduction wall resistances of the evaporator and condenser, respectively; R_2 and R_3 are the evaporation and boiling resistances, respectively; R_4 is the saturated vapor resistance from the vapor flow pressure drop; R_5 is the condensation resistance at the condenser; R_7 is the axial conduction thermal resistance; R_8 and R_9 are the evaporation and condensation liquid-vapor interfacial thermal resistances, respectively. For ideal thermosyphon operation, the temperature drop from the evaporator ($T_{s,E}$) to the bottoming cycle application (T_c) should be small.

The TEs selected for HSTE analysis are bismuth telluride (Bi_2Te_3), lead telluride (PbTe), and silicon germanium (SiGe), which have a range of operating temperatures with moderate *ZTs* (Figure 3), relatively low cost, and commercial availability (Minnich et al., 2009; Poudel et al., 2008). Based on the TE and bottoming cycle application temperatures (T_c), different combinations of thermosyphon wall materials-working fluid are considered that ensure working fluid compatibility and high effective thermal conductivity. Conventional water-copper (300 K –550 K), mercury-stainless steel (550 K – 875 K), and liquid potassium-nickel (885 K – 1273 K) thermosyphons were investigated for Bi_2Te_3 (300 K – 525 K), PbTe (525 K – 850 K), and SiGe (850 K – 1200 K) TEs, respectively. The PbTe and SiGe HSTEs are suitable for medium to high temperature IPH applications, while Bi_2Te_3 HSTEs can be used for low temperature IPH or residential heating. The TE module contains negligible spacing between the TE legs such that only conduction heat transfer through the TE legs is considered (Rockendorf et al., 2000; Li et al., 2010).

2.2 GOVERNING EQUATIONS

We solved the energy equation governing the thermoelectric and thermosyphon over a wide range of input parameters including solar concentration, TE and thermosyphon material and geometry, thermosyphon working fluid, and bottoming cycle temperature. All transport properties vary with temperature including the TE thermal conductivity (k_{te}), figure of merit (*ZT)*, thermosyphon wall thermal conductivity (k_w), and thermosyphon fluid properties (k_v, k_l, μ_v, μ_l, σ, ρ_v, ρ_l, C_{pv}, C_{pl}, h_{fg}). Figures 4a and 4b show schematics of the thermosyphon evaporator and condenser, respectively, which include the energy inputs and outputs in the system.

[Figure 4]

At the TE side (Figure 4a), the energy gained from the solar heat input (Q_{solar}) and lost from emissive loss (Q_{out}) is balanced by the generated TE power (P_{te}) and waste heat (Q_{out})

$$\underbrace{\alpha A_{CS} C G}_{\text{Solar Heat Input } (Q_{solar})} - \underbrace{\sigma_B \varepsilon A_E (T_{ss}{}^4 - T_\infty{}^4)}_{\text{Radiative Loss } (Q_{loss})} = \underbrace{P_{te}}_{\text{TE Power}} + \underbrace{Q_{out}}_{\text{Waste Heat}} \quad (1)$$

where C is the solar concentration ratio, A_{SC} is the evaporator cross sectional area ($2r_{te}L_e$), A_E is the evaporator surface area ($2\pi r_{te}L_e$), G is the average solar insolation (1000 W/m^2), α and ε are the selective surface spectrally averaged solar absorbtivity and thermal emissivity, respectively, σ_B is the Stefan-Boltzmann constant, T_{ss} is the selective surface and TE hot side temperature, and T_∞ is the ambient temperature (300 K). The TE power is defined as

$$P_{te} = (Q_{solar} - Q_{loss}) \cdot \eta_{te} = (Q_{solar} - Q_{loss}) \cdot \frac{T_{ss} - T_{s,E}}{T_{ss}} \frac{\sqrt{1 + \overline{ZT}} - 1}{\sqrt{1 + \overline{ZT}} + \frac{T_{s,E}}{T_{ss}}} \quad (2)$$

where η_{te} is the TE electrical generation efficiency, $T_{s,E}$ is the TE cold side temperature, and ZT is the thermoelectric figure of merit. The TE material properties were averaged over the operating temperature interval [T_{ss}, $T_{s,E}$]. At the thermosyphon condenser side (Figure 4b), the energy transferred from the evaporator (Q_{out}) is transferred directly to the bottoming cycle application at the condenser temperature (T_c).

2.3 THERMOSYPHON MODELING

The thermosyphon is modeled using a thermal resistance network, $R = \Delta T/Q$, where R is the thermal resistance, ΔT is the temperature difference across each thermal resistance, and Q is the heat transfer (Figure 2b). The resistances are determined for low (T < 500 K) and high (T > 500 K) temperature operating regimes (Table 1). At low temperatures, classical Nusselt condensation/evaporation film theory (Faghri, 1995; Incropera and DeWitt, 1985) is used. However, at high temperatures with liquid metals as the working fluid, high vapor velocities result in large interfacial shear stresses and additional interfacial heat transfer resistances (R_8 and R_9) at the liquid vapor interface. Therefore, a modified Nusselt analysis with pool boiling and thin film evaporation (Sukhatme and Rohsenow, 1966; Faghri, 1995; Da Cunha and Mantelli, 2006; Da Cunha and Mantelli, 2009) more effectively captures the phase-change at the evaporator. In all cases, the ratio of condensate film thickness (δ) and tube radius (r_i) is assumed to be very small ($\delta/r_i \ll 1$), such that the tube can be modeled as laminar film condensation on a flat inclined surface.

[Table 1]

Low Temperature Thermosyphon Model ($T_{s,E}$ < 550 K)

We considered Nusselt film condensation and evaporation for a specified condenser outer wall temperature (T_c) to obtain the temperature distribution of low temperature thermosyphons, where the thermal resistances are given by Eqns. 3 – 12. For small thermosyphon length to radii ratios ($L_c/r_i \leq 20$), the thermosyphon tube is modeled as laminar film condensation on a flat inclined surface, where the condensed film returns to the evaporator by gravity and evaporates completely by the end of the evaporator section (*i.e.,* no liquid pool exists at the base of the

evaporator). However, for larger length to radii ratios (L_c/r_i > 20), a modified heat transfer coefficient correlation is used that better captures the circumferential liquid film thickness variation due to thermosyphon inclination (Hussein, 2001). The vapor is assumed to be at saturation conditions, and shear forces are negligible (Faghri, 1995) resulting in thermal resistances of evaporation and condensation heat transfer described by Eqns. 5 and 8, respectively.

To determine the difference in saturation temperature from the evaporator ($T_{sat,E}$) to condenser ($T_{sat,C}$), the Clapeyron relation is used which accounts for the vapor flow thermal resistance (Eqn. 4). While previous works have found this resistance to be negligible (Prasher, 2003), the moderate heat fluxes and temperatures in this analysis can lead to appreciable temperature drops.

High Temperature Thermosyphon Model ($T_{s,E}$ > 550 K)

At higher temperatures, the interfacial shear stresses can create significant error in the predicted film thickness profile using classical Nusselt theory. Therefore, a separate high temperature model is used to predict thermosyphon performance using a modified Nusselt model with pool boiling heat transfer, where the thermal resistances are given by Eqns. 13 – 22. For simplicity, we also assume that the evaporator and wall temperatures are uniform and use the modified Nusselt condensation model in the condenser section (Da Cunha and Mantelli, 2006; Da Cunha and Mantelli, 2009) with the addition of liquid vapor interfacial resistances (R_8 and R_9).

To determine the liquid vapor interfacial resistances (Eqns. 21 and 22), we assume condensation and evaporation coefficients (σ) of 0.1 which is appropriate for large engineering systems which typically are difficult to maintain in a pure environment (Sukhatme and Rohsenow, 1966). The film evaporation heat transfer coefficient from the top of the evaporator section to the liquid pool is

$$\bar{h}_{f,E} = \frac{g\cos\theta\rho_l(\rho_l-\rho_v)h_{fg}}{3\mu_l\left(T_{sat,E}-T_{w,E}\right)\left(L_e-L_p\right)}\left[\left(A\left(L_t-L_p\right)+{\delta_{L_0}}^4-A(L_c+L_a)\right)^{\frac{3}{4}}-{\delta_{L_0}}^3\right] \tag{23}$$

$$\delta_{L_o} = \left[\frac{4k_l\mu_l(T_{sat,C}-T_{w,C})L_c}{g\cos\theta\rho_l(\rho_l-\rho_v)h_{fg}}\right]^{\frac{1}{4}}, \qquad A = \frac{4k_l\mu_l(T_{sat,E}-T_{w,E})}{g\cos\theta\rho_l(\rho_l-\rho_v)h_{fg}}$$

where δ_{Lo} is the film thickness at the end of the adiabatic section, L_p is the length of the pool region, L_e is the evaporator length, L_c is the condenser length, and L_t is the total length of the thermosyphon (Da Cunha and Mantelli, 2009). Eqn. 23 is combined with Eqn. 15 to determine the effective thermal resistance of the thin film liquid metal evaporation.

To incorporate the effect of pool boiling of liquid metals, the heat transfer coefficient is determined by

$$\bar{h}_{p,E} = Cq^{0.7}{P_r}^m \tag{25}$$

where $P_r = P_l/P_c$, $C = 13.7$, $m = 0.22$ for $Pr < 0.001$, and $C = 6.9$, $m = 0.12$ for $Pr > 0.001$, q is the evaporator heat flux, P_c is the critical pressure of the liquid metal, and P_l is the liquid pressure in contact with the heated surface. (Shah, 1992) This average heat transfer coefficient is used with Eqn. 16 to determine the effective thermal resistance due to liquid metal pool boiling (R_3).

For both low and high temperature thermosyphon models, we assume operation below limiting thermosyphon operating conditions. To verify this assumption, the continuum, sonic, viscous, entrainment, and boiling limits (Faghri, 1995; Dickerson, 1996) are calculated and compared with the corresponding operational performance (see Appendix). In addition, non-condensable gases are assumed to be in negligible amounts as to not affect the heat transfer characteristics. We also verified that the film condensation is laminar using the condensation Reynolds number ($Re_\delta < 30$). The transient response of the HSTE is not considered due to the relatively low thermal mass and quick startup time of thermosyphons and evacuated tube solar collectors (Mather, 1982; Faghri, 1995; de Winter, 1991).

2.4 SOLUTION ALGORITHM

The HSTE model was solved iteratively where the solar concentration (C), bottoming cycle temperature (T_c), TE and thermosyphon geometry and materials and thermosyphon working fluid are input parameters to obtain the temperature distribution ($[T]$), thermoelectric power (P_{te}), waste heat (Q_{out}), emissive loss (Q_{loss}) and system efficiency. To determine the transport properties ($[P]_O$), a guessed initial temperature distribution ($[T]_O$) is used. Once initial properties are obtained, the model iterates to determine a new temperature distribution ($[T]_1$) by solving the energy equation (Eqn. 1) with thermal resistances (Eqns. 3 – 22). The transport properties ($[P]_1$) are recalculated with the new temperature distribution and used in the next iteration. The convergence criterion is defined as when the difference between successive temperatures for each point is less than 0.01 degrees ($|T_{i+1} - T_i| < 0.01$) (see Appendix). The choice of materials for the thermosyphon and TE is made based on the calculated temperature distribution in each successive iteration.

3. RESULTS AND DISCUSSION

3.1 MODEL RESULTS

The modeling results were obtained for a particular solar collector resembling the glass tube evacuated design ($L_e = 50$ cm, $L_c = 10$ cm, $L_a = 200$ cm, $r_o = 2.25$ cm, $r_i = 2$ cm, $r_{te} = 3$ cm, $\theta = 30°$) with black chrome as the selective surface which is stable at high temperatures (300 K – 800 K) (see Appendix). Also, the emissivity is relatively high ($0.08 < \varepsilon < 0.3$) compared to other selective surfaces, allowing for a conservative estimate of performance. Figure 5a

shows the bottoming cycle heat transfer (Q_{out}) as a function of bottoming cycle temperature (T_c) and solar concentration (C). Three distinct regimes for different TEs exist with T_c. When the TE or thermosyphon temperatures exceed 550 K, the PbTe TE with the mercury-stainless steel thermosyphon replaces the Bi_2Te_3 TE with the water-copper thermosyphon, creating a discontinuity in the system performance. These discontinuities are larger at higher *Cs* because a larger temperature difference exists at higher heat fluxes. A similar shift occurs at $T_{s,E} > 778$ K to a SiGe TE with the liquid potassium-nickel thermosyphon. As the C increases, the shift occurs at a lower T_c because the thermosyphon temperature drop is greater, leading to a higher cold side TE temperature. As a result, Bi_2Te_3 HSTE systems at high *Cs* have a very narrow operation window (300 K < T_c < 340 K).

Figure 5b shows the emissive loss (Q_{loss}) as a function of T_c, C, and TE material. As C increases, the selective surface temperature (T_{ss}) increases, leading to higher emissive loss. Therefore, the decrease in Q_{out} (Figure 5a) is more pronounced at $T_c > 500$ K due to the fourth order dependence of emissive losses on temperature. Figure 5c shows the output TE power as a function of T_c, C, and TE material. The TE efficiency is dependent on the temperature difference ($T_{ss} - T_{w,E}$) across the TE module and figure of merit (ZT) (Section 1). As T_c increases, P_{te} decreases due to a decrease in Q_{out}. With higher C, however, a higher temperature difference across the TE element can be attained due to the higher heat flux, leading to a higher power output (P_{te}).

[Figure 5]

Figure 6 shows the thermosyphon evaporator wall temperature ($T_{w,E}$) as a function of condenser temperature (T_c) and solar concentration (C). The difference between evaporator and condenser temperature is larger in the low temperature regime due to the higher thermosyphon heat transfer and lower emissive losses. Additionally, low temperature copper water thermosyphons have lower effective heat transfer coefficients than high temperature liquid metal thermosyphons due to the lower thermal conductivity, surface tension and latent heat of vaporization of water.

[Figure 6]

Inclination angles from the vertical (θ) up to 30° were examined and show a small effect on the performance of the HSTE system (< 2%). For inclination angles up to 70°, the thermosyphon can still operate without significant deterioration (< 10%) which agrees well with previous experiments and theory (Negishi and Sawada, 1983; Hahne and Gross, 1981). Once the thermosyphons are inclined to greater than 70°, they cannot be used for HSTE system integration due to poor performance. Similarly, the thermosyphon adiabatic section length (L_a) shows minimal effect (< 0.1%) on performance at low condenser temperatures (T_c < 550 K) and solar concentrations (C < 50), indicating that the saturation temperature drop associated with the vapor pressure drop in the thermosyphon is negligible in these regimes. However, as discussed in Section 1.3, the saturation temperature drop needs to be considered in liquid metal HSTE systems due to a significant vapor pressure drop at high solar concentration ratios.

3.2 HSTE OPTIMIZATION

To appropriately select the highest performance solution for a given application, optimization of the HSTE system is needed. The HSTE is optimized based on a combination of two efficiencies: 1) the electrical efficiency (η_{te}) defined as the TE efficiency (Eqn. 2) and 2) the thermal efficiency (η_c) from waste heat (Q_{loss}) defined using an exergetic approach with the Carnot efficiency (Eqn. 26) (Rosen et al., 2004)

$$\eta_c = \left(1 - \frac{T_\infty}{T_c}\right). \tag{26}$$

The defined thermal efficiency serves as an ideal upper limit to the amount of work obtained from the waste heat if a heat engine is used as the bottoming cycle. The overall system efficiency (η_{HSTE}) is therefore defined as the ratio of useful energy extracted, including the thermal (Q_{out}) and electrical components (P_{te}), compared to the total energy input (see Appendix for full derivation)

$$\eta_{HSTE} = \frac{\text{Useful Energy Out}}{\text{Incident Solar Energy}} = (\eta_{te} + \eta_c - \eta_{te}\eta_c)\left(1 - \frac{Q_{loss}}{CG}\right). \tag{27}$$

[Figure 7]

Figure 7 shows the HSTE efficiency as a function of bottoming cycle temperature and solar concentration. Similar to Figure 5, discontinuities due to temperature operation limits of the TE and thermosyphon exist (see Section 3.1). To obtain HSTE efficiency for a particular bottoming cycle application, the end use temperature at which the thermal energy will be transferred to must be known. For example, if the HSTE system is to be used for space heating, the temperature is set to the condenser temperature (T_c), and the system performance can be obtained from Figure 7.

Effect of Bottoming Cycle Temperature (T_c) and Concentration (C): Figure 7 shows that the HSTE efficiency (η_{HSTE}) has optimal values as a function of bottoming cycle temperature (T_c). The initial increase is due to the increase in thermal efficiency with increasing temperature. However, as T_c continues to increase, the surface temperature (T_{ss}) of the TE element reaches a point where the emissive losses (Q_{loss}) begin to dominate. As a result, with any additional increase in T_c, the efficiency decreases due to the fourth order temperature dependence of the emissive losses. At constant T_c, the system efficiency (η_{HSTE}) increases with increasing solar concentration (C) due to higher heat transfer (Q_{out}) through the thermosyphon and greater thermal efficiency. Concentrations beyond 100 suns may be more advantageous but may have economic implications on the construction of the concentrator; and therefore were not considered here.

Effect of TE Leg Length (L_{te}) and Thermosyphon Size (r_o/r_{te}): Figure 8a examines the HSTE system efficiency with TE leg length (L_{te}) and cross-sectional radii ratio (r_i/r_{te}) for a particular solar concentration (C = 50) and bottoming cycle temperature (T_c = 700 K) determined from Figure 7. As L_{te} increases, the system efficiency decreases due to the additional thermal resistance of the TE leg, leading to an elevated surface temperature (T_{ss}) and higher emissive loss (Q_{loss}). The TE leg length, however, has different effects on system performance depending on the bottoming cycle temperature (T_c). At high T_c, small increases in L_{te} result in larger decreases in system efficiency due to the higher emissive losses at increasing temperatures. However, Figure 8b shows that the TE power increases with increasing TE leg length because collector area increases and a higher TE temperature gradient exists. Depending on the power needs of the application, increasing TE leg length may have advantages. For example, if the application has larger electrical demands, it may be more favorable to sacrifice overall system efficiency for electrical production.

Figure 8 also shows that as the radial ratio of the thermosyphon (r_o/r_{te}) decreases for a constant L_{TE}, the system efficiency decreases due to reduced area for heat transfer through the thermosyphon and the TE power decreases due to reduced selective surface area for solar input. As the TE leg length increases, the maximum operating temperature (776 K) is reached, and the performance decreases to zero (gray area). In addition, for small thermosyphon radii (bottom white area), heat pipe limitations (*e.g.*, sonic limit) prohibit operation. Furthermore, as the thermosyphon radius becomes less than r_o ~ 2 mm, the model is no longer accurate because the thermosyphon pipe wall cannot be modeled as a flat plate. Similar investigations on geometry were performed for other optimal C and T_c values, and show comparable results (see Appendix).

[Figure 8]

Effect of Thermosyphon Material: In an effort to broaden thermosyphon material selection, we investigated the effect of thermosyphon wall thermal conductivity (k_w) on performance. Only the low temperature model was considered due to material compatibility issues for high temperature liquid metals. Figure 9 shows the HSTE system efficiency (η_{HSTE}) as a function of solar concentration (C) and thermosyphon wall thermal conductivity (k_w) for a Bi_2Te_3 TE at T_c = 470 K. As k_w decreases from 10 W/mK, the efficiency does not decrease appreciably, which indicates that the radial conduction resistance of the thermosyphon wall is not dominant. However, as the thermal conductivity decreases below approximately 1.2 W/mK, system efficiency begins to decrease more significantly from the efficiency at high k_w values (η^*). The results indicate that materials such as glass can be used for thermosyphons in HSTE systems when solar concentrations are below 4 suns, which can reduce material costs (Window and Harding, 1984). A glass thermosyphon design can be integrated into a bottoming cycle process via a header and manifold design most commonly seen in current solar thermal applications (Zhiqiang, 2005; Window and Harding, 1984).

[Figure 9]

To achieve the optimal HSTE system for a prescribed bottoming cycle using the framework described above, the following procedure should be followed: 1) An initial geometry should be specified for which an optimum solar

concentration and bottoming cycle temperature can be determined (*e.g.,* Figure 7). 2) The thermosyphon and TE geometry should be optimized based on results from step 1 (*e.g.,* Figure 8). 3) A new geometry can then be selected that meets the power and heat requirements of the particular application. 4) Steps 1 to 3 need to be repeated until convergence is reached. In practice, system constraints such as the bottoming cycle temperature and solar concentration are specified, which simplifies the optimization routine to geometry only. Step 4 was not needed for this study because the geometry of interest was specified.

Five applications for HSTE systems are proposed in Table 2 showing applications requiring relatively high heat output compared to electrical power production, such as residential heating, solar AC, and industrial process heating, are ideal for HSTE integration. The results also demonstrate the applicability of HSTEs for high temperature applications such as chemical drying and aluminum smelting, previously not possible with existing PVT systems.

[Table 2]

4. CONCLUSIONS

A hybrid solar thermoelectric system using a thermosyphon to efficiently transport heat for a bottoming cycle (HSTE) was studied over a wide range of temperatures (300 K – 1200 K), solar concentrations (1 – 100 suns), as well as thermosyphon and TE materials and geometries. An energy-based model for the TE and thermosyphon was developed to predict the temperature distribution to determine the performance of the HSTE system. The results show that HSTE system efficiency is a strong function of solar concentration and bottoming cycle temperature due to the coupling between temperature and thermosyphon performance, TE performance and selective surface properties. As the bottoming cycle temperature increases, the thermal efficiency increases to an optimum critical temperature. Beyond this temperature, the emissive losses dominate, resulting in a decrease in HSTE efficiency. As solar concentration increases, both thermal and thermoelectric efficiencies increase due to higher heat fluxes to the HSTE. Geometric optimization of the HSTE also shows at higher TE leg lengths and radii ratios, higher levels of electrical power and waste heat could be obtained but with decreased efficiency. A range of optimum efficiencies were determined, the highest of which include: 34.4% (T_c = 500 K, C = 50), 48.1% (T_c = 700 K, C = 100), and 52.6% (T_c = 776 K, C = 100). The results from varying the thermosyphon wall material show when wall thermal conductivities exceed 1.2 W/mK, system efficiency is approximately constant, indicating glass thermosyphons could be used for low temperature (T < 550 K) HSTEs to potentially reduce material cost. The outcomes of this study indicate a major benefit of using the HSTE system where unlike PVT systems, they can be utilized at high temperatures while maintaining electrical conversion efficiencies comparable to or greater than room temperature operation. The development of the HSTE system extends the applicability of hybrid solar thermal to higher temperature processes such as chemical drying and aluminum smelting, which mainly require mainly high quality heat. This study serves as a framework for selection and optimization of HSTE system configuration based on the end use application.

5. NOMENCLATURE

A	Area [m^2]
C	Solar concentration factor [-]
C_p	Specific heat capacity [J/kg-K]
C_s	Pool boiling constant [-]
g	Gravitational constant [N/kg]
G	Incident radiative heat flux [W/m^2]
h	Heat transfer coefficient [W/m-K]
h_{fg}	Latent heat of vaporization [J/kg]
$h_{f,E}$	Evaporator thin film evaporation heat transfer coefficient [W/m-K]
$h_{p,E}$	Evaporator liquid metal pool boiling heat transfer coefficient [W/m-K]
k	Thermal conductivity [W/m-K]
L_a	Adiabatic section length [m]
L_c	Condenser section length [m]
L_e	Evaporator section length [m]
L_f	Evaporator thin film length [m]
L_o	Total thermosyphon length [m]
L_p	Liquid metal pool height [m]
L_{te}	Thermoelectric leg length [m]
M	Molecular mass [kg/kmol]
$\dot{m}$	Mass flux [kg/m^2-s]
P	Pressure [Pa]
P_c	Critical pressure [Pa]
P_l	Liquid pressure [Pa]
P_r	Reduced pressure [-]
P_{te}	Thermoelectric power [W]
q	Heat flux [W/m^2]
Q_{loss}	Emissive loss [W]
Q_{out}	Bottoming cycle heat transfer [W]
Q_{solar}	Solar heat input [W]
r_i	Thermosyphon inner radius [m]
r_o	Thermoelectric inner radius, thermosyphon outer radius [m]
r_{te}	Thermoelectric outer radius [m]
R_1	Evaporator wall radial thermal resistance [K/W]
R_2	Evaporator liquid pool thermal resistance [K/W]
R_3	Evaporator thin film thermal resistance [K/W]
R_4	Vapor core axial thermal resistance [K/W]
R_5	Condenser film thermal resistance [K/W]
R_6	Condenser wall radial thermal resistance [K/W]
R_7	Condenser wall axial thermal resistance [K/W]
R_8	Liquid metal thin film evaporation interfacial thermal resistance [K/W]
R_9	Liquid metal condensation interfacial thermal resistance [K/W]
R_{te}	Thermoelectric element radial thermal resistance [K/W]
R	Gas constant [J/kg-K]
$\bar{R}$	Universal gas constant [J/kmol-K]
s	Pool boiling constant [-]
t	Thermosyphon wall thickness [m]
T	Temperature [K / °C]
T_c	Condenser outer wall / bottoming cycle temperature [K]
$T_{s,E}$	Thermosyphon evaporator outer wall temperature, thermoelectric cold side temperature [K]
$T_{sat,E}$	Thermosyphon evaporator saturation temperature [K]
$T_{sat,C}$	Thermosyphon condenser saturation temperature [K]
T_{ss}	Selective surface / thermoelectric hot side temperature [K]
$T_{vl,E}$	Thermosyphon evaporator liquid vapor interface temperature [K]
$T_{vl,C}$	Thermosyphon condenser liquid vapor interface temperature [K]
$T_{w,E}$	Thermosyphon evaporator inner wall temperature [K]
$T_{w,C}$	Thermosyphon condenser inner wall temperature [K]
T_∞	Environment temperature [K]
x,y	Coordinates [m]

Greek Symbols

α Absorbtivity [-]
ε Emissivity [-]
η Efficiency [-]
η^* Efficiency as $k_w \rightarrow \infty$ [-]
ρ_R Reflectivity [-]
ρ Density [kg/m^3]
σ_B Stefan-Boltzmann constant [W/m-K^4]
σ Surface tension [N/m]
σ' Condensation coefficient [-]
τ Transmissivity [-]
μ Dynamic viscosity [Pa-s]
δ Liquid film thickness [m]
θ Thermosyphon inclination angle from the vertical [deg.]

Superscript
DC Direct current
HSTE Hybrid solar thermoelectric system
IPH Industrial process heat
PV Photovoltaic
PVT Hybrid photovoltaic thermal
SS Selective Surface
TE Thermoelectric
ZT Thermoelectric figure of merit
$\bar{}$ Mean or average value

Subscripts
a Adiabatic
bb Black body
c, C Condenser
e, E Evaporator
HSTE Hybrid solar thermoelectric system
l Liquid medium
L_o Total length of adiabatic and condenser section [m]
p,E Pool boiling at the evaporator
p Liquid pool
ss Selective surface
sat Saturation conditions
t Total
te Thermoelectric
th Thermal
v Vapor medium
vl Liquid vapor interface
w Wall

ACKNOWLEDGEMENTS

This material is based upon work supported as part of the MIT S3TEC Center, and Energy Frontier Research Center funded by the Department of Energy, Office of Science, Office of Basic Energy Sciences. Nenad Miljkovic would also like to acknowledge funding support from the Natural Sciences and Engineering Research Council of Canada.

ROLE OF THE FUNDING SOURCE

Funding for this research was provided by the MIT S3TEC Center, and Energy Frontier Research Center (funded by the Department of Energy, Office of Science, Office of Basic Energy Sciences) and the Natural Sciences and

Engineering Research Council of Canada. Funding sources had no involvement in the study design; the collection, analysis, and interpretation of data; the writing of this report; and in the decision to submit the paper for publication.

DISCLOSURE STATEMENT

The authors disclose that there is no conflict of interest including financial, personal or other relationships with other people or organizations that could inappropriately influence (bias) the work.

6. REFERENCES

Buffet, P., 1982. Hybrid thermal and photovoltaic concentration collector. EC Contractors meeting, Brussels.

Chen, G., 2011. Theoretical efficiency of solar thermoelectric energy generators. Journal of Applied Physics, 109, 104908

Chowdhury, I., Otanicar, T., Prasher, R., Sherbeck, J., Phelan, P., Burrell, M., 2010. Enhanced Efficiency in a Coupled Photovoltaic/Thermal Concentrating Solar Collector. Proceedings of the ASME 4th International Conference on Energy Sustainability, 529-536.

Clausse, M., Alarn, K.C.A., Meunier, F., 2008. Residential air conditioning and heating by means of enhanced solar collectors coupled to an adsorption system. Solar Energy, 82, 885-892.

Coventry, J.S., 2004. Performance of a concentrating photovotaic/thermal solar collector. Solar Energy, 78, 211-222.

Da Cunha, A. F. V., Mantelli, M.B.H., 2009. Analytical and Experimental Analysis of a High Temperature Mercury Thermosyphon. Journal of Heat Transfer, 131, -.

Da Cunha, A. F. V., Mantelli, M.B.H., 2006. Modeling of High Temperature Thermosyphons. Proceedings of the 9th AIAA/ASME Joint Thermophysics and Heat Trasnfer Conference.

De Winter, F., 1991. Solar Collectors, Energy Storage, and Materials. The MIT Press, Boston, MA.

Davidson, J.H., 2005. Low-temperature solar thermal systems: An untapped energy resource in the United States. Journal of Solar Energy Engineering, 127, 305-306.

Demeter, C.P., Gray, E.E., Carwile, C., 1991. Estimating the Potential for Solar Thermal Applications in the Industrial-Process Heat Market 1990-2030. Proceedings of the 26th International Energy Conversion Engineering Conference, E133-E138.

Deng, Y.G., Liu, J., 2009. Recent advances in direct solar thermal power generation. Journal of Renewable and Sustainable Energy, 1(5), -.

Desideri, U., Proietti, S., Sdringola, P., 2009. Solar-powered cooling systems: Technical and economic analysis on industrial refrigeration and air-conditioning applications. Applied Energy, 86, 1376-1386.

Dickerson, T.J., 1996. Performance Analysis of a Liquid Metal Heat Pipe Space Shuttle Experiment. Department of the Air Force Air University Masters Thesis, 78.

Dubey, S., Tiwari, G.N., 2008. Thermal modeling of a combined system of photovoltaic thermal (PV/T) solar water heater. Solar Energy, 82, 602-612.

El Fadar, A., Mimet, A., Perez-Garcia, M., 2009. Modelling and performance study of a continuous adsorption refrigeration system driven by parabolic trough solar collector. Solar Energy, 83, 850-861.

El-Sharkawy, A.A., Kenawy, M.I., Hillal, A.S., Abu-Basha, H.M., 1983. Thermophysical Properties of Polycrystalline PbS, PbSe, and PbTe in Temperature Range 300 - 700 K. International Journal of Thermophysics, 4, 261-269.

Faghri, A., 1995. Heat Pipe Science and Technology. Taylor & Francis, Washington, DC.

Fong, K.F., Chow, T.T., Lee, C.K., Lin, Z., Chan, L.S., 2010. Comparative study of different solar cooling systems for buildings in subtropical city. Solar Energy, 84, 227-244.

Garg, H.P., Adhikari, R.S., 1999. System performance studies on a photovoltaic/thermal (PV/T) air heating collector. Renewable Energy, 16, 725-730.

Gibart, C., 1981. Study of and tests on a hybrid photovoltaic-thermal collector using concentrated sunlight. Solar Cells, 4, 71-89.

Grass, C., Schoelkopf, W., Staudacher, L., Hacker, Z., 2004. Comparison of the optics of non-tracking and novel types of tracking solar thermal collectors for process heat applications up to 300 degrees C. Solar Energy, 76, 207-215.

Green, M.A., 2003. General temperature dependence of solar cell performance and implications for device modelling. Progress in Photovoltaics, 11, 333-340.

Hahne, E., Gross, U., 1981. The influence of the inclination angle on the performance of a colased two-phase thermosyphon. Heat Recovery Systems, 1, 267-274.

Han, J.Y., Mol, A.P.J., Lu, Y.L., 2010. Solar water heaters in China: A new day dawning. Energy Policy, 38, 383-391.

Hussein, H.M.S., Mohamad, M.A., El-Asfouri, A.S., 2001. Theoretical analysis of laminar-film condensation heat trasnfer inside inclined wickless heat pipes flat-plate solar collector. 23, 525-535.

Incropera, F.P., DeWitt, D.P., 1985. Fundamentals of Heat and Mass Transfer. Wiley, New York.

Kalogirou, S., 2003. The potential of solar industrial process heat applications. Applied Energy, 76, 337-361.

Kelso, J.D., 2008-2009 Buildings Energy Data Book. US Department of Energy

Kennedy, C.E., Price, H., 2006. Progress in development of high-temperature solar-selective coating. Solar Engineering 2005, 749-755.

Kramer, D., Poudel, B., Feng, H.P., Caylor, J.C., Yu, B., Yan, X., Ma, Y., Wang, X., Wang, D., Muto, A., McEnaney, K., Chiesa, M., Ren, Z., Chen, G., 2011. High-performance flat-panel solar thermoelectric generators with high thermal concentration. Nature Metrials, 10, 532-538.

Kribus, A., Mittelman, G., 2008. Potential of polygeneration with solar thermal and photovoltaic systems. Journal of Solar Energy Engineering, 130, -.

Kulkarni, G.N., Kedare, S.B., Bandyopadhyay, S., 2008. Design of solar thermal systems utilizing pressurized hot water storage for industrial applications. Solar Energy, 82, 686-699.

Lecuona, A., Ventas, R., Venegas, M., Zacarias, A., Salgado, R., 2009. Optimum hot water temperature for absorption solar cooling. Solar Energy, 83, 1806-1814.

Lenoir, B., Dauscher, A., Poinas, P., Scherrer, H., Vikhor, L., 2003. Electrical performance of skutterudites solar thermoelectric generators. Applied Thermal Engineering, 23, 1407-1415.

Lertsatitthanakorn, C., Therdyothin, A., Soponronnarit, S., 2010. Performance analyses and economic evaluation of a hybrid thermoelectric solar water heater. Journal of Power and Energy, 224, 621-627.

Li, P., Cai, L.L., Zhai, P.C., Tang, X.F., Zhang, Q.J., Niino, M., 2010. Design of a Concentration Solar Thermoelectric Generator. Journal of Electronic Materials, 39, 1522-1530.

Lienhard, J.H., Dhir, V.K., 1973. Extended Hydrodynamic Theory of the Peak and Minimum Heat Fluxes, NASA CR-2270

Luque, A., Marti, A., 1999. Limiting efficiency of coupled thermal and photovoltaic converters. Solar Energy Materials and Solar Cells, 58, 147-165.

Manuel, R., Reiner, B., James, E.P., 2002. An Update on Solar Central Receiver Systems, Projects, and Technologies. Journal of Solar Energy Engineering, 124, 98-108.

Mather, G.R., 1982. Transient Response of Solar Collectors. Journal of Solar Energy Engineering, 104, 165-172.

Minnich, A.J., Dresselhaus, M.S., Ren, Z.F., Chen, G., 2009. Bulk nanostructured thermoelectric materials: current research and future prospects. Energy & Environmental Science, 2, 466-479.

Morelli, D.T., Jovovic, V., Heremans, J.P., 2008. Intrinsically minimal thermal conductivity in cubic I-V-VI2 semiconductors. Physical Review Letters, 101, -.

Murray, J.P., 1999. Aluminum production using high-temperature solar process heat. Solar Energy, 66, 133-142.

Muto, A., Chen, G., 2010. Thermoelectric Topping Cycle for Trough Solar Thermal Power Plant. Proceedings of the Materials Research Society Symposium, Boston, MA, 1218.

Negishi, K., Sawada, T., 1983. Heat transfer performance of an inclined two-phase colsed thermosyphon. International Journal of Heat and Mass Transfer, 26, 8, 1207-1213.

Omer, S.A., Infield, D.G., 1998. Design optimization of thermoelectric devices for solar power generation. Solar Energy Materials and Solar Cells, 53, 67-82.

Pacheco, J.E., 2001. Demonstration of solar-generated electricity on demand: The Solar Two project. Journal of Solar Energy Engineering, 123, 5-5.

Poudel, B., Hao, Q., Ma, Y., Lan, Y.C., Minnich, A., Yu, B., Yan, X.A., Wang, D.Z., Muto, A., Vashaee, D., Chen, X.Y., Liu, J.M., Dresselhaus, M.S., Chen, G., Ren, Z.F., 2008. High-thermoelectric performance of nanostructured bismuth antimony telluride bulk alloys. Science, 320, 634-638.

Prasher, R.S., 2003. A simplified conduction based modeling scheme for design sensitivity study of thermal solution utilizing heat pipe and vapor chamber technology. Journal of Electronic Packaging, 125, 378-385.

Rockendorf, G., Sillmann, R., Podlowski, L., Litzenburger, B., 1999. PV-hybrid and thermoelectric collectors. Solar Energy, 67, 227-237.
Rosell, J.I., Vallverdu, X., Lechon, M.A., Ibanez, M., 2005. Design and simulation of a low concentrating photovoltaic/thermal system. Energy Concersion and Management, 46, 3034-3046.
Rosen, M.A., Le, M.N., Dincer, I., 2004. Exergetic analysis of cogeneration-based district energy systems. Journal of Power and Energy, 218, 369-375.
Schnitzer, H., Brunner, C., Gwehenberger, G., 2007. Minimizing greenhouse gas emissions through the application of solar thermal energy in industrial processes. Journal of Cleaner Production, 15, 1271-1286.
Shah, M.M., 1992. A Survey of Experimental Heat-Transfer Data for Nucleate Pool Boiling of Liquid-Metals and a New Correlation. International Journal of Heat and Fluid Flow, 13, 370-379.
Shahsavar, A., Ameri, M., 2010. Experimental investigation and modeling of a direct-coupled PV/T air collector. 84, Solar Energy, 1938-1958.
Sherman, A., Martinek, F., 1961. The Thermodynamic and Electrical Properties of Mercury Vapor at Pressures Below Atmospheric and High Temperatures. Planetary and Space Science, 271-282
Snyder, G.J., Toberer, E.S., 2008. Complex thermoelectric materials. Nature Materials, 7, 105-114.
Sukhatme, S.P., Rohsenow, W.M., 1966. Heat Transfer during Film Condensation of a Liquid Metal Vapor. Journal of Heat Transfer, 88, 19-&.
Tripanagnostopoulos, Y., 2007. Aspects and improvements of hybrid photovoltaic/thermal solar energy systems. Solar Energy, 81, 1117-1131.
Tripanagnostopoulos, Y., Nousia, T., Souliotis, M., Yianoulis, P., 2002. Hybrid photovoltaic/thermal solar systems. Solar Energy, 72, 217-234.
Tundee, S., Terdtoon, P., Sakulchangsatjatai, P., Singh, R., Akbarzadeh, A., 2010. Heat extraction from salinity-gradient solar ponds using heat pipe heat exchangers. Solar Energy, 84, 1706-1716.
Window, B., Harding, G.L., 1984. Progress in the Materials Science of All-Glass Evacuated Collectors. Solar Energy, 32, 609-623.
Xi, H.X., Luo, L.G., Fraisse, G., 2007. Development and applications of solar-based thermoelectric technologies. Renewable and Sustainable energy Reviews, 11, 923-936.
Zhiqiang, Y., 2005. Development of solar thermal systems in China. Solar Energy Materials and Solar Cells, 86, 427-442.
Zondag, H.A., 2005. Flat-plate PV-Thermal collectors and systems: A review. Renewable and Sustainable Energy Reviews, 12, 891-959.

ALL FIGURES ARE INTENDED FOR COLOR REPRODUCTION ON THE WEB AND IN PRINT.

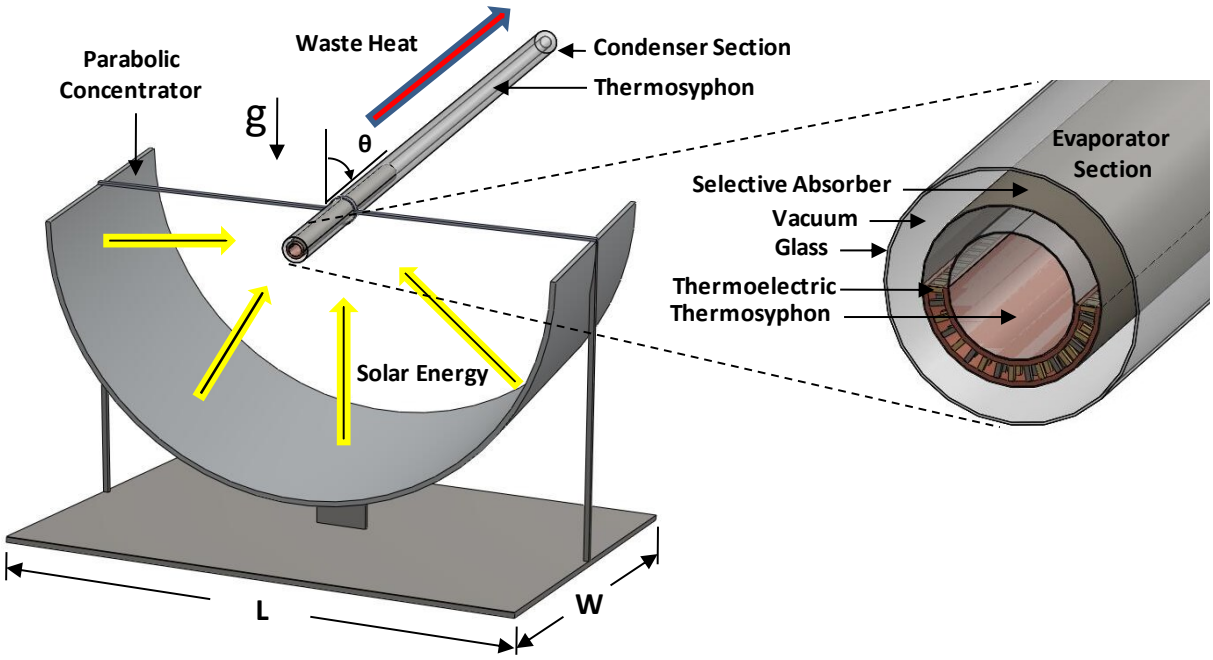

Figure 1. Schematic of the hybrid solar thermoelectric system (HSTE). Solar energy is focused by a parabolic concentrator on the evaporator section of the evacuated tube absorber (thermosyphon), which heats the TE hot side. The resulting temperature difference between the TE hot and cold sides produces electrical power while heat carried away (waste heat) by the thermosyphon (adjacent to the cold side) is transferred to the condenser section for the bottoming cycle.

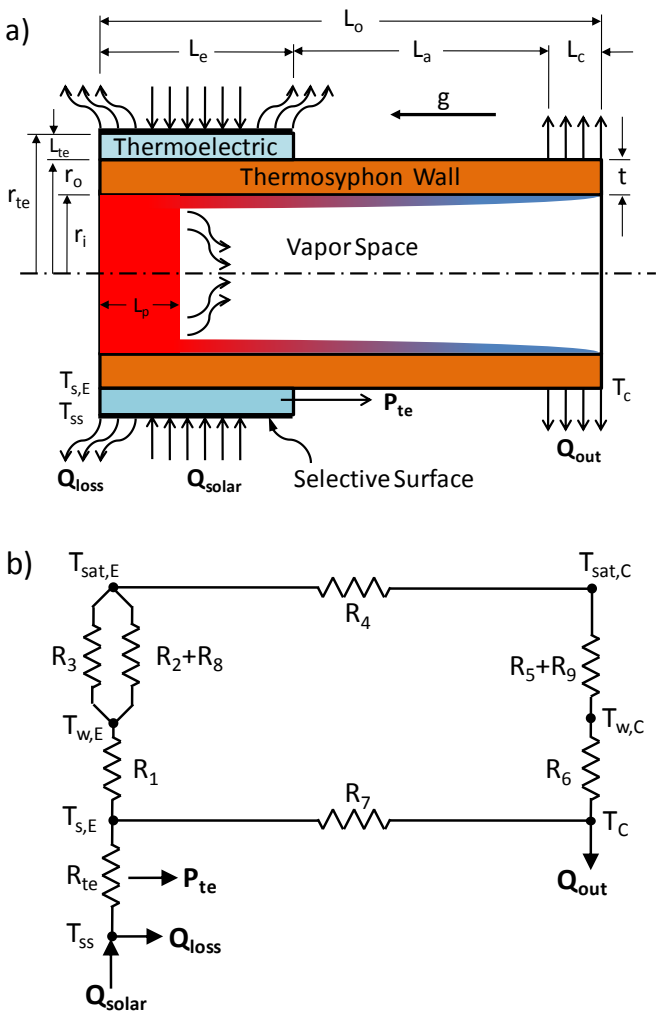

Figure 2. (a) Schematic cross-section of the HSTE system in a horizontal orientation. Solar energy (Q_{solar}) heats the selective surface located on the TE hot side, which creates a temperature gradient across the TE that produces electrical power (P_{te}). The remaining heat (Q_{out}) is transferred axially by the thermosyphon to a bottoming cycle application at temperature T_c. (b) Thermal resistance (TR) model of the HSTE, where R_{te} is the TE radial TR, R_1 and R_6 are the thermosyphon wall radial TR, R_2 and R_3 are the boiling and evaporation TRs, respectively, R_5 is condensation TR, R_4 is the vapor TR, R_7 is the thermosyphon wall axial TR, and R_8 and R_9 are evaporation and condensation interfacial TRs, respectively.

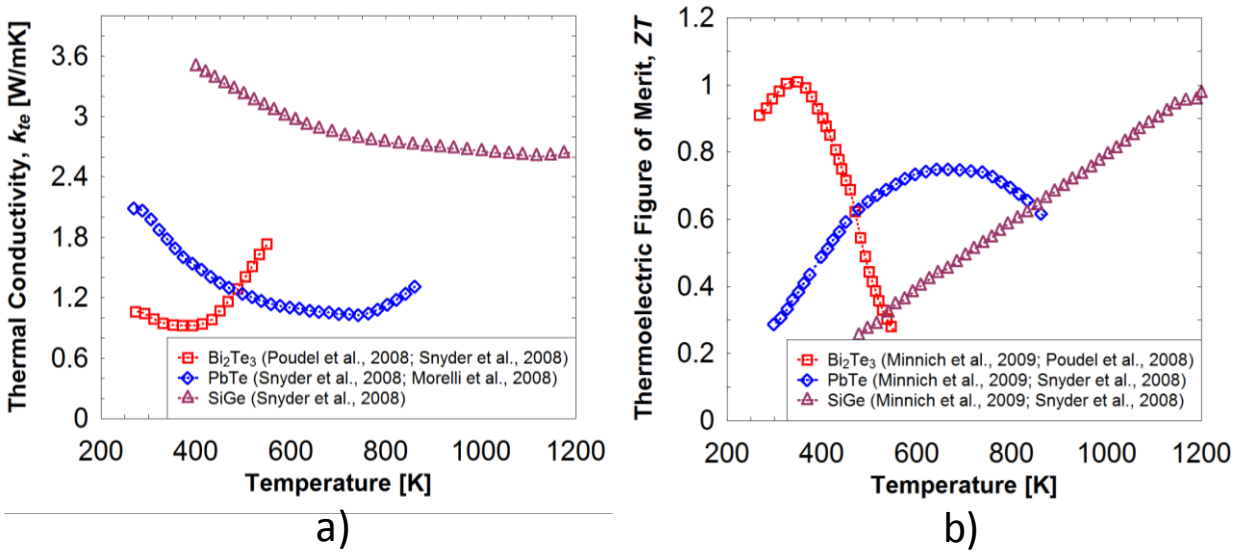

Figure 3. Thermoelectric (a) thermal conductivity (k_{te}) and (b) figure of merit (ZT) as a function of temperature for three TE materials used for the model: bismuth telluride (Bi_2Te_3), lead telluride (PbTe) and silicon germanium (SiGe) (Minnich et al., 2009; Snyder and Toberer, 2008; Poudel et al., 2008).

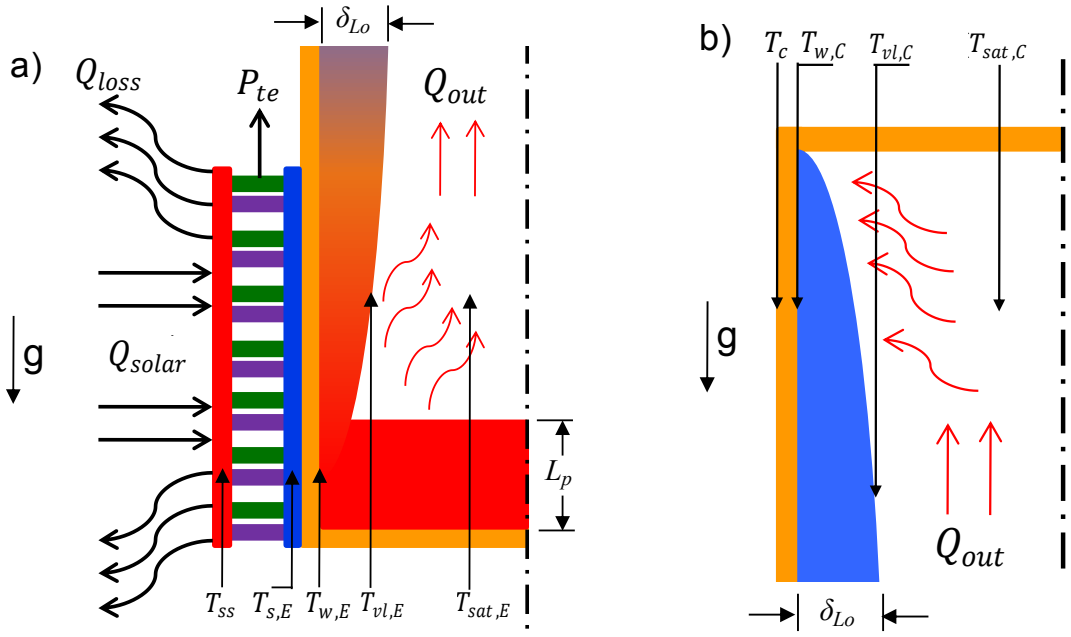

Figure 4. Schematics of the (a) TE side showing the film evaporation and pool boiling region of the evaporator and (b) condenser side showing film condensation in a vertical orientation. Energy inputs and outputs are labeled.

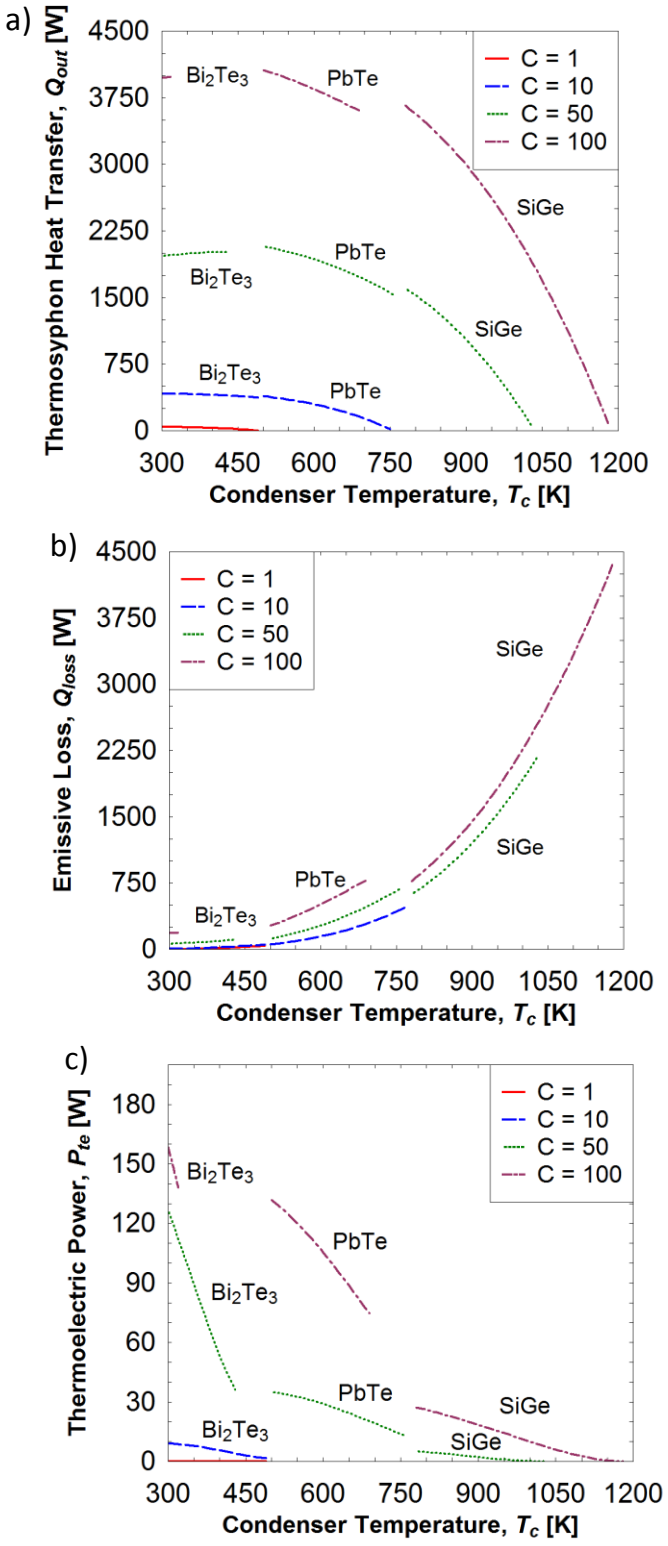

Figure 5. a) Thermosyphon heat transfer, b) emissive losses and c) TE power of the HSTE system for varying solar concentrations and condenser temperatures. As the condenser temperature (T_c) increases, emissive losses (Q_{loss}) increase while TE power (P_{te}) and thermosyphon waste heat (Q_{out}) decrease due to the increased surface temperatures (T_{ss}). As solar concentration (C) increases, emissive losses, TE power and heat output increase.

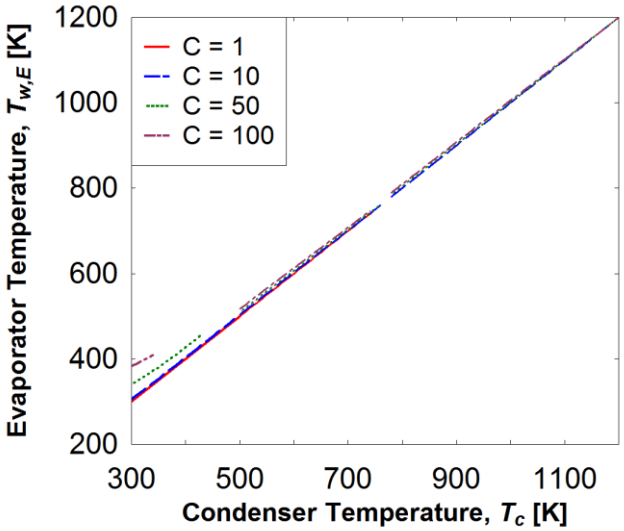

Figure 6. Thermosyphon evaporator temperature for varying solar concentrations and condenser temperatures. As the condenser temperature (T_c) increases, emissive losses (Q_{loss}) increase while thermosyphon waste heat (Q_{out}) decreases resulting in smaller temperature drop across the thermosyphon. As solar concentration (C) increases, the heat output increases, resulting in a larger temperature drop. Additionally, liquid metal thermosyphons show smaller temperature drops due to more efficient heat transfer.

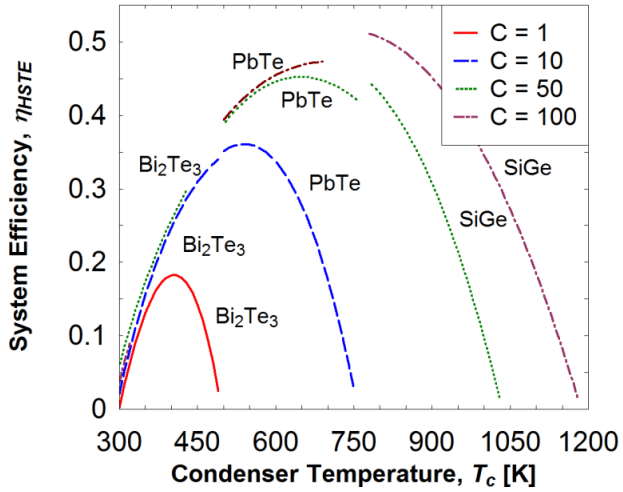

Figure 7. Efficiency of the HSTE system for varying solar concentrations (C) and bottoming cycle temperatures (T_c). Optimal system efficiencies exist which balance the thermal efficiency and emissive power. Increasing the solar concentration also increases efficiency due to a higher energy input and thermal efficiency.

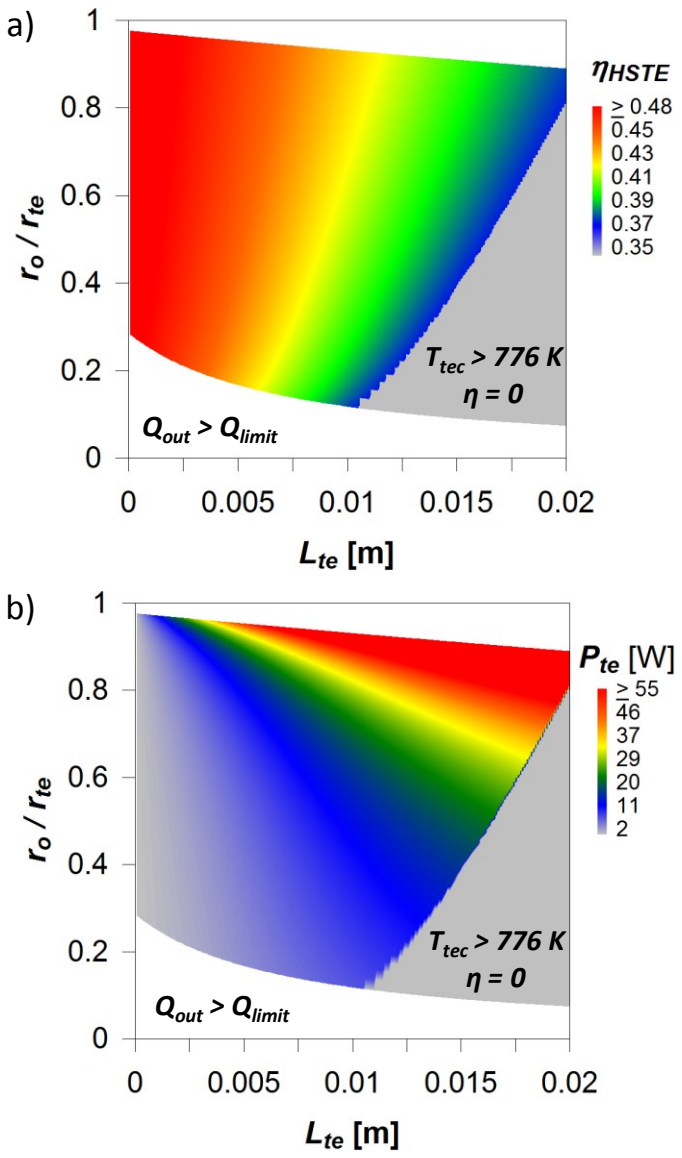

Figure 8. Optimization results for a PbTe HSTE at $C = 50$ and $T_c = 700$ K showing a) system efficiency and b) TE power. An increase in TE leg length (L_{te}) decreases efficiency and increases TE power due to a larger TE thermal gradient. As the TE leg length increases, the maximum operating temperature (776 K) is reached, at which point the performance decreases to zero (gray area). In addition, for small thermosyphon radii (bottom white area), heat pipe limitations (*e.g.*, sonic limit) prohibit operation.

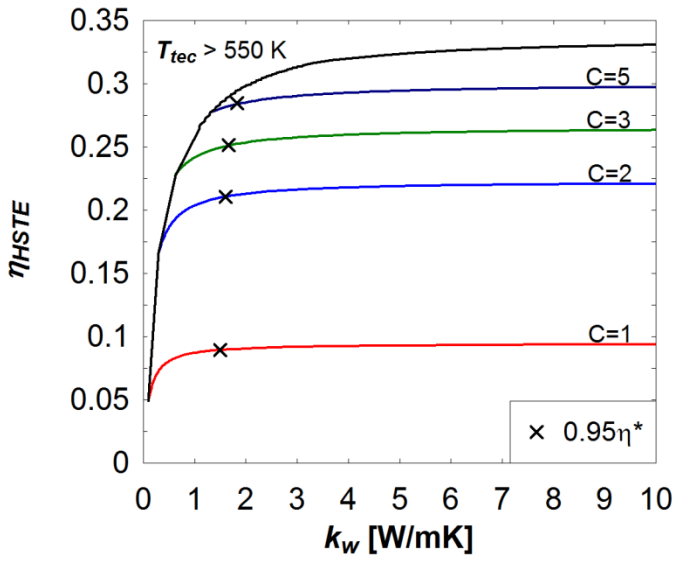

Figure 9. HSTE system efficiency for varying solar concentrations (C) and thermosyphon wall thermal conductivities (k_w) for a Bi_2Te_3 TE at T_c = 470 K. η* is the HSTE efficiency at high thermal conductivities (η* = $\eta_{HSTE}(k_w = 10$ W/mK)), which asymptotes to a constant value. For solar concentrations below 4 suns, materials with thermal conductivities larger than 1.2 W/mK have comparable system performance (η* ~ η_{HSTE}).

Table 1 – Thermal Resistances for Low and High Temperature HSTE Models

Low Temperature Model (T < 500 K)		High Temperature Model (T > 500 K)	
$R_{te} = \frac{\ln\left(\frac{r_{te}}{r_o}\right)}{2\pi L_e k_{te}}$	(3)	$R_{te} = \frac{ln\left(\frac{r_{te}}{r_o}\right)}{2\pi L_e k_{te}}$	(13)
$R_1 = \frac{\ln\left(\frac{r_o}{r_i}\right)}{2\pi L_e k_w}$	(4)	$R_1 = \frac{ln\left(\frac{r_o}{r_i}\right)}{2\pi L_e k_w}$	(14)
$R_2 = \frac{1}{2\bar{h}_E \pi r_i L_e}$ $\bar{h}_E = 0.943\left[\frac{\rho_l g cos\theta(\rho_l-\rho_v)h_{fg}{k_l}^3}{\mu_l(T_{w,E}-T_{sat,E})L_E}\right]^{\frac{1}{4}} \quad \frac{L_E}{r_i} \le 20$ $\bar{h}_E = A\left[\frac{\rho_l g(\rho_l-\rho_v)h_{fg}{k_l}^3}{\mu_l(T_{w,E-T_{sat,E}})L_E}\right]^{\frac{1}{4}} \quad \frac{L_E}{r_i} > 20$ $A = [0.997 - 0.334(cos\theta)^{0.108}]\left[\frac{L_E}{2r_i}\right]^{[0.254(cos\theta)^{0.108}]}$	(5)	$R_2 = \frac{1}{2\bar{h}_{E,f}\pi r_i(L_e - L_p)}$	(15)[a]
$R_3 = 0$	(6)	$R_3 = \frac{1}{(2\pi r_i L_p + \pi {r_i}^2)\bar{h}_{E,p}}$	(16)[b]
$R_4 = \frac{8L_o R\mu_v\left(\frac{T_{sat,E}-T_{sat,C}}{2}\right)^2}{\pi {h_{fg}}^2 p_v \rho_v {r_i}^4}$	(7)	$R_4 = \frac{8L_o R\mu_v\left(\frac{T_{sat,E}-T_{sat,C}}{2}\right)^2}{\pi {h_{fg}}^2 p_v \rho_v {r_i}^4}$	(17)
$R_5 = \frac{1}{2\bar{h}_C \pi r_i L_c}$ $\bar{h}_C = 0.943\left[\frac{\rho_l g cos\theta(\rho_l-\rho_v)h_{fg}{k_l}^3}{\mu_l(T_{sat,C}-T_{w,C})L_C}\right]^{\frac{1}{4}} \quad \frac{L_C}{r_i} \le 20$ $\bar{h}_C = A\left[\frac{\rho_l g(\rho_l-\rho_v)h_{fg}{k_l}^3}{\mu_l(T_{sat,C}-T_{w,C})L_C}\right]^{\frac{1}{4}} \quad \frac{L_C}{r_i} > 20$ $A = [0.997 - 0.334(cos\theta)^{0.108}]\left[\frac{L_C}{2r_i}\right]^{[0.254(cos\theta)^{0.108}]}$	(8)	$R_5 = \frac{1}{2\bar{h}_C \pi r_i L_c}$ $\bar{h}_C = 0.943\left[\frac{\rho_l g cos\theta(\rho_l-\rho_v)h_{fg}{k_l}^3}{\mu_l(T_{sat,C}-T_{w,C})L_C}\right]^{\frac{1}{4}} \quad \frac{L_C}{r_i} \le 20$ $\bar{h}_C = A\left[\frac{\rho_l g(\rho_l-\rho_v)h_{fg}{k_l}^3}{\mu_l(T_{sat,C}-T_{w,C})L_C}\right]^{\frac{1}{4}} \quad \frac{L_C}{r_i} > 20$ $A = [0.997 - 0.334(cos\theta)^{0.108}]\left[\frac{L_C}{2r_i}\right]^{[0.254(cos\theta)^{0.108}]}$	(18)
$R_6 = \frac{\ln\left(\frac{r_o}{r_i}\right)}{2\pi L_c k_w}$	(9)	$R_6 = \frac{\ln\left(\frac{r_o}{r_i}\right)}{2\pi L_c k_w}$	(19)
$R_7 = \frac{\frac{1}{2}(L_e + L_c) + L_a}{\pi({r_0}^2 - {r_i}^2)k_w}$	(10)	$R_7 = \frac{\frac{1}{2}(L_e + L_c) + L_a}{\pi({r_0}^2 - {r_i}^2)k_w}$	(20)
$R_8 = 0$	(11)	$R_8 = \left(\frac{\sigma'}{2-\sigma'}\right)\left(\frac{2}{\pi}\right)^{\frac{1}{2}}\left(\frac{M}{\bar{R}}\right)^{\frac{3}{2}}\frac{P_{sat,E}h_{fg}}{{T_{sat,E}}^{\frac{5}{2}}}$ * See text for definition calculation of σ	(21)
$R_9 = 0$	(12)	$R_9 = \left(\frac{\sigma'}{2-\sigma'}\right)\left(\frac{2}{\pi}\right)^{\frac{1}{2}}\left(\frac{M}{\bar{R}}\right)^{\frac{3}{2}}\frac{P_{sat,C}h_{fg}}{{T_{sat,C}}^{\frac{5}{2}}}$ * See text for definition calculation of σ	(22)

a) See text for definition of $h_{E,f}$
b) See text for definition of $h_{E,p}$

Table 2. HSTE Potential Applications and Performance (Per Unit Length of Evaporator Section)

HSTE Application	η_{HSTE} [%]	T_c [K]	C	P_{te} [W/m]	Q_{out} [kW/m]
Residential Heating	15.2	360	50	200	4
Solar Air Conditioning [a)]	25.4	400	50	100	4
Low temperature IPH - Chemical Drying [b)]	34.4	500	100	250	7.6
Medium Temperature IPH [c)]	48.1	700	100	140	7
High Temperature IPH - Aluminum Smelting [d)]	52.6	776	100	60	7.5

a) Clausse et al., 2008; Desideri et al., 2009; El Fadar et al., 2009; Fong et al., 2010; Lecuona et al., 2009
b) Demeter et al., 1991; Kalogirou, 2003
c) Grass et al., 2004; Kulkarni et al., 2008
d) Funken et al., 1999; Murray, 1999

Appendix

Selective Surface Properties

NREL data (Kennedy and Price, 2006) was used to estimate the emissive losses and solar absorption by the selective surface. The emissivity of the selective surface as a function of temperature is shown in Figure A.1. For temperatures exceeding the maximum tabulated temperature, a 6th order polynomial was used to extrapolate the properties at the higher temperature. While black chrome cannot be used at high temperatures, other selective surface materials, *i.e.*, Ni:SiO_2 (α = 0.93, ε = 0.14 at 1000 to 1100 K) or MbOc + M'Fe_2O_4 (α > 0.9, ε = 0.45 at 1000 K), have similar radiative properties to that of black chrome when extrapolated to higher temperatures. The absorbtivity of the selective surface is shown in Table A.1. The spectrally-averaged emissivity is measured independently of the absorbtivity. The absorbtivity is calculated through a reflectance measurement using the AM1.5 (1 kW/m^2) solar spectrum at normal incidence.

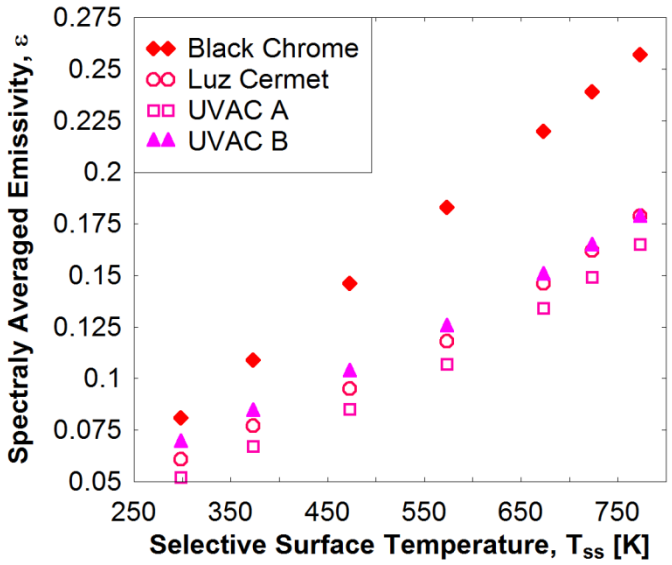

Figure A.1. Spectrally averaged emissivity as a function of selective surface temperature (T_{ss}) for four commercially available surface coatings (Kennedy and Price, 2006).

Table A.1. Spectrally Averaged Absorbtivity.

	Black Chrome	Luz Cermet	UVAC A	UVAC B
Solar α	0.916	0.938	0.954	0.935

Heat Transfer Limitations

Although thermosyphons are efficient heat transfer devices, they are subject to operating limits that determine their maximum heat transfer. The limit that has the lowest value at a specific operating condition causes failure of the thermosyphon (Faghri, 1995). The results were all checked against the operating limits.

The vapor continuum limit (Dickerson, 1996), applicable to high temperature liquid metal thermosyphons, occurs when the heat transfer is not high enough to form continuum flow conditions inside the thermosyphon. The vapor temperature associated with transition into continuum flow is

$$T_{continuum} = \frac{2\sqrt{2}\pi d^2 P_v Knr_i}{1.051k} \tag{A.1}$$

where d is the effective molecular diameter of the liquid metal atom, P_v is the liquid metal vapor pressure, Kn is the Knudsen number, r_i is the thermosyphon inner radius, and k is the Boltzmann constant. The effective molecular diameters for potassium and mercury are 4.44 Å and 3.02 Å, respectively (Dickerson, 1996; Sherman and Martinek, 1961). The vapor flow is considered to be continuum when $Kn < 0.01$. We determine the continuum temperature for each simulated result and ensure it is higher than the evaporator ($T_{sat,E}$) and condenser ($T_{sat,C}$) saturation temperatures. In all cases, the continuum limit temperature is well below saturated vapor temperatures in the system.

The sonic limit occurs at the evaporator of the thermosyphon as a result of the pressure driven liquid metal vapor acceleration towards the evaporator end. The low downstream vapor pressure of the liquid metal thermosyphon during startup can lead to sonic vapor velocities at the evaporator exist (Faghri 1995). The heat transfer corresponding to the sonic limit is

$$Q_{sonic} = \pi {r_i}^2 h_{fg} \rho_{sat,E} \left[\frac{\frac{C_{p,g}}{C_{v,g}} RT_{sat,E}}{2(\frac{C_{p,g}}{C_{v,g}} + 1)} \right]^{\frac{1}{2}} \tag{A.2}$$

where $C_{p,g}$ and $C_{v,g}$ are the heat capacities of the liquid metal vapor at the evaporator conditions, and R is the working fluid gas constant (Sherman and Martinek, 1961).

The viscous limit describes the maximum heat transfer that the thermosyphon can experience before the viscous forces of the vapor flow begin to overcome the inertial forces from the evaporator to the condenser. This limitation was checked using

$$Q_{viscous} = \frac{\pi {r_i}^4 h_{fg} \rho_{sat,E} P_{sat,E}}{16 \mu L_o} \tag{A.3}$$

where h_{fg} is the latent heat of evaporation of the working fluid, $\rho_{sat,E}$ and $P_{sat,E}$ are the evaporator vapor density and pressure, respectively, L_o is the effective thermosyphon length, and μ is the evaporator vapor dynamic viscosity.

The entrainment limit occurs when the vapor flow rate is high enough to entrain some of the back flowing liquid moving down the thermosyphon. This limitation is more predominant in thermosyphons containing wick structures; however, it was verified for both low and high temperature thermosyphon models using

$$Q_{entrainment} = \left(\frac{\rho_l}{\rho_v}\right)^{0.14} tanh^2 Bo^{\frac{1}{4}} h_{fg} \pi {r_i}^2 \left(g\sigma(\rho_l - \rho_v)\right)^{\frac{1}{4}} \left({\rho_v}^{-\frac{1}{4}} + {\rho_l}^{-\frac{1}{4}}\right)^{-2} \quad \text{(A.4)}$$

where *Bo* is the Bond number, σ is the working fluid surface tension, ρ_l and ρ_v are the densities of the liquid and vapor, respectively (Faghri, 1995). All properties were evaluated at the evaporator saturation temperature.

The boiling limit describes when the evaporator surface temperature ($T_{w,E}$) exceeds the superheat corresponding to the critical heat flux (CHF), resulting in catastrophic failure of the thermosyphon. The boiling limit is determined by

$$Q_{boiling} = \ (2\pi r_i L_e) 0.149 \rho_v h_{fg} \left[\frac{\sigma g(\rho_l - \rho_v)}{{\rho_v}^2}\right]^{\frac{1}{4}} \quad \text{(A.5)}$$

where L_e is the evaporator length, and r_i is the thermosyphon inner radius (Lienhard and Dhir, 1973). Equation A.5 is applicable to liquid metals as a conservative estimate since the experimentally measured CHF for the boiling of liquid metal is 2 to 4 times higher than that predicted by the equation (Lienhard and Dhir, 1973).

HSTE System Efficiency Derivation

The ideal thermoelectric efficiency η_{te} is used to determine the TE electrical power output

$$P_{te} = \eta_{te}\left(Q_{solar} - \sigma\varepsilon A_E\left({T_{ss}}^4 - {T_\infty}^4\right)\right) = \frac{T_{ss} - T_{s,E}}{T_{ss}} \frac{\sqrt{1+\overline{ZT}} - 1}{\sqrt{1+\overline{ZT}} + \frac{T_{s,E}}{T_{ss}}} \left(Q_{solar} - \sigma\varepsilon A_E\left({T_{ss}}^4 - {T_\infty}^4\right)\right). \quad \text{(A.6)}$$

The electrical power from the waste heat (W_{cg}) is given by

$$W_{cg} = \eta_c \left(Q_{solar} - P_{te} - \sigma\varepsilon A_E\left({T_{ss}}^4 - {T_\infty}^4\right)\right) \quad \text{(A.7)}$$

where η_c is the ideal Carnot efficiency ($\eta_c = 1\text{-}T_c/T_\infty$) and T_∞ is the ambient temperature (300 K).

To obtain the overall HSTE system efficiency, the two components of the useful energy output (P_{te}, W_{cg}) are combined and compared to the total energy input

$$\eta_{HSTE} = \frac{P_{te} + W_{cg}}{Q_{solar}} \tag{A.8}$$

Substituting Eqns. A.6 and A.7 into A.8, we obtain

$$\eta_{HSTE} = \frac{\eta_{te}\left(Q_{solar} - \sigma\varepsilon A_E\left({T_{ss}}^4 - {T_\infty}^4\right)\right) + \eta_c\left(Q_{solar} - \sigma\varepsilon A_E\left({T_{ss}}^4 - {T_\infty}^4\right) - \eta_{te}\left(Q_{solar} - \sigma\varepsilon A_E\left({T_{ss}}^4 - {T_\infty}^4\right)\right)\right)}{Q_{solar}} \tag{A.9}$$

where C is the solar concentration, G_S is the solar heat flux (1000 W/m^2), A_E is the absorber surface area, and ε is the absorber emissivity.

By simplifying A.9, the system efficiency is expressed as

$$\eta_{HSTE} = (\eta_{te} + \eta_c - \eta_{te}\eta_c)\left(1 - \frac{Q_{loss}}{CG}\right) \tag{A.10}$$

where $Q_{loss} = \sigma\varepsilon A_E({T_{ss}}^4 - {T_\infty}^4)$ represents the radiative loss term. The system efficiency is plotted as a function of bottoming cycle temperature (Figure A.2).

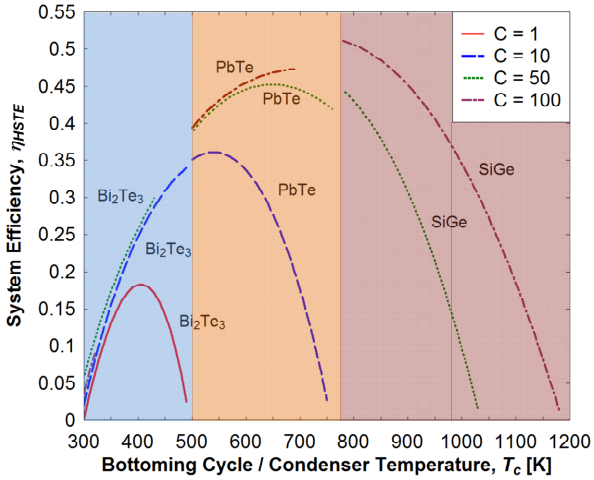

Figure A.2. Efficiency of the HSTE system for varying solar concentrations (C) and bottoming cycle temperatures (T_c). Optimal system efficiencies exists which balance the thermal efficiency (η_c) and emissive losses (Q_{loss}). Increasing the solar concentration (C) also increases efficiency due to higher energy input and thermal efficiency. The blue, orange and red regions corresponding to a Bi_2Te_3 TE/water copper thermosyphon, a PbTe TE/mercury stainless steel thermosyphon, and a SiGe TE/potassium nickel thermosyphon, respectively.

Solution Algorithm

The HSTE numerical model was solved iteratively using the convergence criterion such that the difference between successive temperatures is less than 0.01 degrees ($|T_{i+1}-T_i| < 0.01$). Figure A.3 shows the flowchart of the iterative algorithm used in the model.

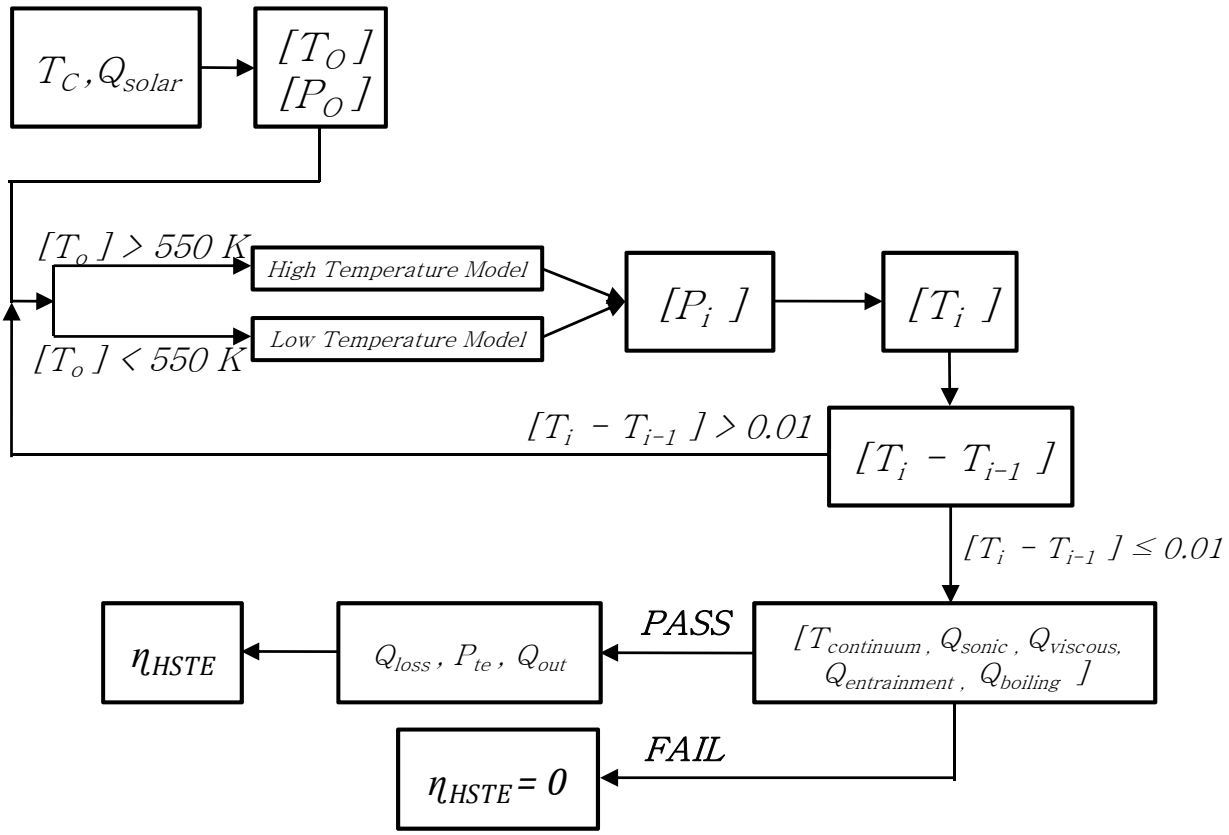

Figure A.3. Flowchart of the iterative algorithm. [T_o] is the initially guessed temperature distribution, [P_o] are the initial calculated fluid and thermoelectric properties, *i* is the iteration number, [T_i] is the *i*th iteration temperature distribution, and $T_{continuum}$, Q_{sonic}, $Q_{viscous}$, $Q_{entrainment}$, $Q_{boiling}$ are the thermosyphon limits.

Optimization Results

Figures A.4 and A.5 show the HSTE system performance with TE leg length (L_{te}) and cross-sectional radii ratio (r_i/r_{te}) for two optimal bottoming cycle temperatures and solar concentrations (T_c = 470 K, C = 10 and T_c = 776 K, C = 50) determined from Figure A.3.

As L_{te} increases, the system efficiency decreases due to the additional thermal resistance of the TE leg, leading to an elevated surface temperature (T_{ss}) and higher emissive loss (Q_{loss}). The TE leg length, however, has different effects on system performance depending on the bottoming cycle temperature (T_c). At high T_c, small increases in L_{te} result in larger decreases in system efficiency due to the higher emissive losses at higher temperatures. However,

Figures A.4b and A.5b show that the TE power increases with increasing TE leg length because collector area increases and a higher TE temperature gradient exists.

Figures A.4 and A.5 also show that as the radii ratio of the thermosyphon (r_o/r_{te}) decreases for a constant L_{TE}, the system efficiency decreases due to reduced area for heat transfer through the thermosyphon and the TE power decreases due to reduced selective surface area for solar input. As the TE leg lengths increases, the maximum operating temperature (500 K) is reached, and the performance decreases to zero (gray area). A gray area is not shown in Figure A.5 because the optimum bottoming cycle temperature is at the low end of the operating temperature range and only exists at $L_{te} > 0.05$. In addition, for small thermosyphon radii (bottom white area), heat pipe limitations (*e.g.*, sonic limit) prohibit operation. Furthermore, as the thermosyphon radius becomes less than $r_o \sim$ 2 mm, the model is no longer accurate because the thermosyphon pipe wall can no longer be modeled as a flat plate.

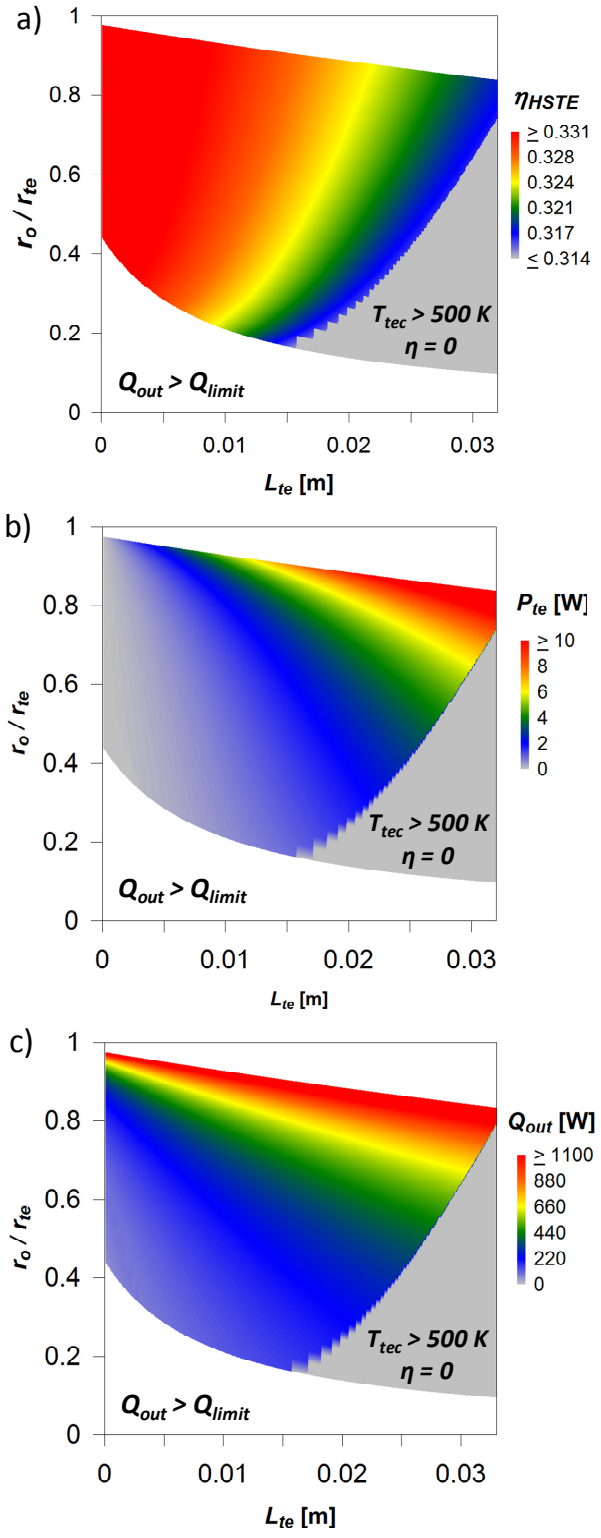

Figure A.4. Optimization results for a Bi_2Te_3 HSTE at $T_c = 470$ K and $C = 10$ showing a) system efficiency, b) TE power, and c) waste heat. An increase in TE leg length (L_{te}) results in a decrease in efficiency and increase in TE power due to a larger TE thermal gradient. As the TE leg length increases, the maximum operating temperature is reached, and the performance decreases to zero (gray area). In addition, for small thermosyphon radii (bottom white area), heat pipe limitations (*e.g.*, sonic limit) prohibit operation.

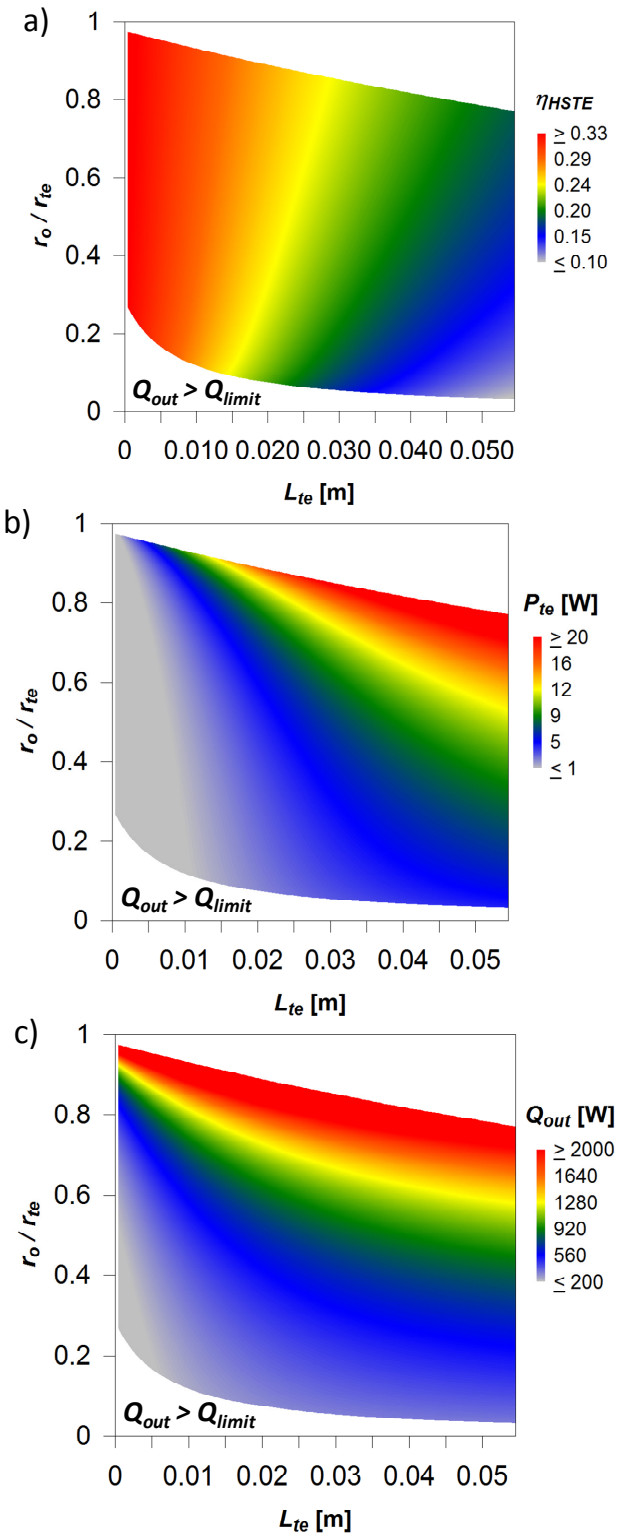

Figure A.5. Optimization results for a SiGe HSTE at T_c = 776 K and C = 50 showing a) HSTE system efficiency, b) TE power and c) waste heat. An increase in TE leg length (L_{te}) results in a decrease in efficiency and increase in TE power due to a larger TE thermal gradient. For small thermosyphon radii (bottom white area), heat pipe limitations (*e.g.*, sonic limit) prohibit operation.